



# Atmospheric ammonia retrieval from the TANSO-FTS/GOSAT thermal infrared sounder

Yu Someya<sup>1</sup>, Ryoichi Imasu<sup>2</sup>, Kei Shiomi<sup>3</sup>, Naoko Saitoh<sup>4</sup>

<sup>1</sup> Center for Global Environmental Research, National Institute for Environmental Studies, Tsukuba, Japan

5 <sup>2</sup>Atmosphere and Ocean Research Institute, the University of Tokyo, Chiba, Japan

<sup>3</sup>Japan Aerospace Exploration Agency, Tsukuba, Japan

<sup>4</sup>Center for Environmental Remote Sensing, Chiba University, Chiba, Japan

*Correspondence to:* Yu Someya (someya.yu@nies.go.jp)

10 **Abstract.** Hyperspectral thermal infrared sounders enable us to grasp the global behavior of minor atmospheric constituents. Ammonia, which imparts large impacts on the atmospheric environment by reacting with other species, is one of them. In this work, we present an ammonia retrieval system that we developed for the Greenhouse Gases Observing Satellite (GOSAT) and the estimates of global atmospheric ammonia concentrations that we derived from 2009 to 2014. The horizontal distributions of the seasonal columnar ammonia concentrations represent significantly high concentrations stemming from six anthropogenic emission source areas and four biomass burning ones. The monthly mean time series of these sites were investigated, and their seasonality was clearly revealed. A comparison with the Infrared Atmospheric Sounding Interferometer (IASI) ammonia product showed a good agreement spatially and seasonally, though there are some differences in detail. The values from GOSAT tend to be slightly larger than those from the IASI for low concentrations, especially in spring and summer. On the other hand, they are lower for particularly high concentrations during summer, such as Eastern China and Northern India. In addition, the largest differences were observed in central Africa. These differences seem to stem from the temporal gaps in observations and the fundamental differences in the retrieval systems.

15  
20

## 1 Introduction

Atmospheric ammonia plays an important role in the nitrogen cycle (Galloway et al., 2004; Behera et al., 2013). Atmospheric nitrogen is taken up by animals and plants and is emitted as a result of their decay or from burning. Ammonia is one of the compounds generated as a byproduct of this process. It is well known that atmospheric ammonia reacts with acids, such as H<sub>2</sub>SO<sub>4</sub> or HNO<sub>3</sub>, and produces nitrate aerosols (e.g., Seinfeld and Pandis, 2016). These aerosols lead to widespread environmental problems, such as the formation of PM<sub>2.5</sub> or PM<sub>10</sub> that is harmful to human health, by changing radiation budgets through the formation of cloud condensation nuclei, and by causing eutrophication through deposition into oceans or lakes.

25



The main emission sources of anthropogenic ammonia into the atmosphere are related to food production (e.g., ammonium-based fertilizers and domestic animals) (Behera et al., 2013). Emissions from these sources have increased along with the growth in the population after industrial evolution. The Emission Database for Global Atmospheric Research (EDGAR) provides several anthropogenic gas emission inventories, including that for ammonia. The analysis of EDGAR-  
5 HYDE data indicated that the annual global emission of ammonia into the atmosphere has increased from 8.6 TgN/yr in 1890 to 43.4 TgN/yr in 1990 (Aardenne et al., 2001). Further, data from EDGAR v4.2 were used to estimate the annual rate of increase in emissions of approximately 0.6 TgN/yr between 1970 and 2008. Biomass burning is also one of the large sources of ammonia emissions. The Global Fire Emissions Database, Version 4 (GFEDv4) (Randerson J.T. and Kasibhatla, 2017) provides information on atmospheric trace gas and aerosol emissions from fire events globally. Ammonia emissions are  
10 estimated using the burned area (Giglio et al., 2013) and an emission factor (Akagi et al., 2011). However, large uncertainties may be associated with these inventories owing to atmospheric ammonia being active and having a short lifetime. Although there are many in situ observations of ammonia, particularly in developed countries and including the Ammonia Monitoring Network (AMoN), it is quite hard to understand the global scale simply using these observational data.

Satellite remote sensing is an effective tool to get a better grasp of the global behavior of atmospheric constituents. Recent  
15 advancements in satellite sensors have allowed us to monitor minor gases, such as greenhouse gases and air pollutants. Currently, the five space-borne nadir satellite sounders, namely, the Atmospheric Infrared Sounder (AIRS), Tropospheric Emission Spectrometer (TES), Infrared Atmospheric Sounding Interferometer (IASI), Thermal and Near-infrared Spectrometer for Observation-Fourier Transform Spectrometer (TANSO-FTS), and Cross-track Infrared Sounder (CrIS), are available to observe atmospheric ammonia. Ammonia has narrow absorption bands in a spectral region of around 10  $\mu\text{m}$ , and  
20 the five sounders measure thermal infrared (TIR) data in this region. The detectable phenomena should differ slightly for each sensor because of the differences in the characteristics of the sensors or because of the orbit paths of the satellites. The frontier work of these sounders for estimating atmospheric ammonia is represented by Beer et al. (2008) using TES data. The authors developed a scaling factor for the ammonia profile and converted it into an averaging kernel weighted molar fraction. Clarisse et al. (2009) revealed the highly spatially resolved global distributions of atmospheric ammonia by converting brightness  
25 temperature differences into columnar concentrations of ammonia in the atmosphere. The sensitivities of the different spectral resolutions and the thermal contrast between surface skin and surface air were investigated by Clarisse et al. (2010). Following these investigations, several other papers have presented results on the global distribution of tropospheric or column-integrated ammonia. Shephard et al. (2011) reported the spatial and seasonal variability on the basis of TES measurements, and they compared them to the GEOS-Chem model simulation. Van Damme et al. (2014, 2015) showed detailed horizontal distributions  
30 and time series derived from the IASI. (Shephard and Cady-Pereira, 2015) investigated the detectability of ammonia and demonstrated the potential retrieval using CrIS data. Warner et al. (2016, 2017) detected ammonia hotspots using AIRS spectra and reported increasing concentrations from agricultural areas. However, some differences in the distributions among the products have been noted but have not been well compared to date.



In this study, atmospheric ammonia was determined using data from the TANSO-FTS on the Greenhouse Gases Observing SATellite (GOSAT). GOSAT observes both the shortwave infrared and the TIR regions simultaneously. Since carbon dioxide (CO<sub>2</sub>) and methane (CH<sub>4</sub>) concentrations have been previously derived from both regions (Yoshida et al., 2011, 2013; Saitoh et al., 2009, 2016), it was possible to calculate the concentrations of ammonia within the same footprint. In Section 2, we will present the details of the satellite data and the retrieval algorithm. In Section 3, the horizontal and temporal distributions of columnar ammonia concentrations derived from the GOSAT are shown. Those results are then compared with the IASI ammonia product, and the differences are discussed.

## 2 Methodology

### 10 2.1 Data and Models

GOSAT was launched into polar orbit on 23 January 2009. With the exception of a few time periods, data have been obtained continuously. The data cover almost the entire globe between about 85°N and 85°S. The equator-crossing time is 13:00 (local time). The TANSO on the GOSAT consists of an FTS and a Cloud and Aerosol Imager (CAI). TANSO-FTS has four bands, of which Band 4 measures the thermal infrared region between 5.5 and 14.3 μm (700–1,800 cm<sup>-1</sup>). Spectral resolution of level 1B (L1B) product is approximately 0.2 cm<sup>-1</sup>. The spectral accuracy of the TIR band of TANSO-FTS has a wavenumber dependency. Kataoka et al. (2013) reported that is 0.5 K at 800 – 900 cm<sup>-1</sup> and 0.1 K at 980 – 1080 cm<sup>-1</sup>. As noting in section 2.2, we assumed that that is 0.3 K in the spectral range used in the ammonia retrieval. This is larger than those of the other hyper-spectral sounders (AIRS: ~0.15 K, IASI: ~0.2 K, CrIS: 0.05 K at 280 K). The instantaneous field of view of the TANSO-FTS is 15.8 mrad circular, which corresponds to approximately a 10.5 km diameter at the earth's surface. TANSO-FTS's scanning system adopts a two-axis pointing mechanism. The maximum pointing angle is ±35° in the cross-track direction and ±20° in the along-track direction (Kuze et al., 2009). With the exception of the target mode or sunglint mode observations over the ocean, the observation pattern was a five-point cross-track scan mode until July 2010 and a three-point cross-track scan mode since August 2010. Since the solar paddle was stopped, the operation of GOSAT was stopped on 24 May 2014. Although the operation of GOSAT restarted on 30 May 2014, the spectral resolution of TANSO-FTS had become slightly lower and the instrument line shape function was changed after the incident (Kuze et al., 2016). In this study, the L1B V160.160 products (Kuze et al., 2012) obtained from the launch to 24 May 2014 provided by the National Institute of Environmental Studies (NIES). Since the magnitude of ammonia emissions to the atmosphere is much higher over land than over the oceans, and because of the computational resources required, only data obtained over land was analyzed. Cloud contaminated scenes were eliminated by CAI cloud screening (Ishida and Nakajima, 2009). The analyzed spectra are only for daytime because CAI is observable during the daytime. In addition to cloud contamination, dust aerosols significantly affected the retrieval of ammonia, because the wavenumber dependence of their optical property is similar to that of ammonia in the



spectral range used in the retrievals. Therefore, the scenes contaminated with dust aerosols in Africa and over other desert surfaces were eliminated using the GOSAT slicing technique (Someya et al., 2016).

Line-By-Line Radiative Transfer Model (Clough et al., 2005) version 12.4, provided by Atmospheric Environmental Research, Inc., was used to calculate the radiative transfer and included gas absorption data obtained from the HIGH-resolution TRANsmission molecular absorption database (HITRAN) 2012 (Rothman et al., 2013). The species of H<sub>2</sub>O, CO<sub>2</sub>, O<sub>3</sub>, N<sub>2</sub>O, CO, CH<sub>4</sub>, and O<sub>2</sub> were considered in the radiative transfer calculations.

The IASI L2 NH<sub>3</sub> product version 2.1 (ANNI-NH3-v2.1) (Van Damme et al., 2017) was used for intercomparison of the results. The previous version of this product was evaluated with the data from ground-based FTS measurements from several sites (Dammers et al., 2016). This product provides ammonia column concentrations for both the morning and the evening. The equator crossing time of the IASI is around 9:30 and 21:30, which are 3 h and 30 min earlier than that of GOSAT. The Interim atmospheric data from the European Centre for Medium-Range Weather Forecasts reanalysis (ERA-Interim) was used for processing this version of the products. The versions of the ERA-Interim were frequently changed, and there were discontinuities among the versions. As a result, the quality and the baseline values of the ammonia column concentrations in the products could vary temporally (Van Damme et al., 2017)

15

## 2.2 Retrieval Algorithm

Ammonia has an antisymmetric stretch mode ( $\nu_3$ ) band around 950 cm<sup>-1</sup>. Figure 1 illustrates the observed GOSAT spectrum over Northern India, its residual between the observed and calculated spectra, and ammonia transmittance. The calculated spectrum was constructed using the retrieved temperature and water vapor profiles. In this study, the band between 960 and 969 cm<sup>-1</sup> was utilized for the retrievals because the band near 930 cm<sup>-1</sup> overlapped with those of the other species. The ammonia retrieval algorithm is based on the nonlinear optimal estimation (Rodgers, 2000) with the Gauss–Newton iteration represented as the following equation:

$$\mathbf{x}_{i+1} = \mathbf{x}_a + (\mathbf{S}_a^{-1} + \mathbf{K}_i^T \mathbf{S}_\epsilon \mathbf{K}_i)^{-1} \mathbf{K}_i^T \mathbf{S}_\epsilon^{-1} [\mathbf{y} - \mathbf{F}(\mathbf{x}_i) + \mathbf{K}_i(\mathbf{x}_i - \mathbf{x}_a)], \quad (1)$$

where  $\mathbf{x}$  is the state vector,  $\mathbf{S}_a$  and  $\mathbf{S}_\epsilon$  are the covariance matrices for a priori and measurements, respectively,  $\mathbf{K}$  is the Jacobian matrix,  $\mathbf{y}$  is the measurement vector,  $\mathbf{F}(\mathbf{x})$  is the forward model vector, and the subscripts  $i$  and  $a$  denote the number of iterations and a priori value, respectively. In this study, the shape of the ammonia mixing ratio profile follows that of the Air Force Geophysics Laboratory (AFGL) atmospheric constituent profiles (Anderson et al., 1986) from which the scaling factor for the profile was retrieved. The standard deviations of the a priori and the measured spectra for ammonia retrievals were assumed to be 20 and 0.3 K, respectively. The ammonia profile of the AFGL profiles and the column averaging kernel for the a priori is shown in Figure 2. If the retrieved scaling factor is negative, the column amount will be recognized as zero. The ammonia profile was scaled using the retrieved scaling factor and converted to a column-integrated mass concentration with the unit of mg/m<sup>2</sup>. The value for the AFGL profile corresponds to approximately 1.325 mg/m<sup>2</sup>.

30



Since temperature and water vapor profiles significantly affect the ammonia retrieval results, they should be considered appropriately. In this study, they are retrieved from the measured spectra in advance of the ammonia retrievals. The retrievals are performed sequentially according to Table 1. The a priori information of temperature and water vapor is estimated from linear temporal and spatial interpolations of the Grid Point Value (GPV) of Global Spectral Model (GSM) products provided by the Japan Meteorological Agency. The GPV (GSM) data are provided for four times per day and have a spatial resolution of 21 layers vertically and  $0.5^\circ \times 0.5^\circ$  grids horizontally. The profiles of  $\text{CO}_2$  and  $\text{CH}_4$  were obtained from the NIES transport model (Saeki et al., 2013). In each retrieval step, the surface temperature was retrieved simultaneously. Surface emissivity was inferred from the Advanced Spaceborne Thermal Emission and Reflection Radiometer Spectral Library (Baldrige et al., 2009) for the land cover types obtained from the MODIS land cover products for each scan (Friedl et al., 2010) based on the International Geosphere-Biosphere Programme land cover classification.

### 3 Results

#### 3.1 Ammonia hotspots and their sources

The horizontal distributions of the columnar ammonia concentrations obtained from the GOSAT within  $2.5^\circ \times 2.5^\circ$  grids for each season (December to February, DJF; March to May, MAM; June to August, JJA; September to November, SON) are shown in Figure 3. The horizontal distribution of hotspots and their seasonal variations are clearly seen in this figure. The values were high in the spring and summer seasons across most of the areas. In Figure 3, significantly high values were observed above several areas such as India, Eastern China, and central Africa. Figure 4 shows the averaged errors with in each grid. The values were excluded when the estimated concentrations were negative. The errors are almost 1.0 to 2.0 [ $\text{mg}/\text{m}^2$ ]. The highconcentration areas are highlighted in Figure 5 and are listed in Table 2. The distribution of these hotspots is quite similar to those previously reported using the IASI (Van Damme et al., 2015) and AIRS (Warner et al., 2016). The largest values were observed in Northern India. In this area, the values were high throughout the year and were more than  $10 \text{ mg}/\text{m}^2$  during JJA. Figure 6 denotes the distributions of the anthropogenic ammonia emissions obtained from the Emission Database for Global Atmospheric Research–Hemispheric Transport of Air Pollution (EDGAR-HTAP) (Janssens-Maenhout et al., 2012) version 2 and GFED4.1s. According to these figures, anthropogenic emissions predominate in India. This area is known to be the strongest anthropogenic ammonia emission source in the world, stemming from agricultural activities, such as livestock and fertilizer applications. The high concentrations also observed in ECH, CUS, and EUR during MAM and JJA are similarly due to agricultural emissions. China, in particular, uses the largest amount of nitrogen fertilizers in the world (Lu and Tian, 2017), as corroborated by the correspondingly high concentrations of ammonia detected. In spite of the smaller emissions indicated by the EDGAR data, the results from the GOSAT show high values in CAS. In this area, the application of nitrogen fertilizers for cotton production has increased, in addition to the number of domesticated sheep (Huang et al., 2012). High concentrations for this area were also noted for in situ observations (Li et al., 2012) and those reported by Van Damme et al.



(2014) using the IASI data and by Warner et al. (2016) using the AIRS data. Hence, the high values obtained from the GOSAT probably reflect these emissions. On the other hand, emissions from biomass burning dominate in SAM, CAF, SAF, and WRU as seen in GFED. Peak values were noted in CAF during MAM and in SAM and SAF during SON. The high values noted in JJA for WRU were a result of large-scale biomass burning that occurred during the disastrous heatwave in 2010. With the exception of CAF, the temporal variations in these areas agreed well with those obtained from the MODIS fire count product (not shown). In CAF, temporal variations are not consistent with the MODIS product, as is discussed in Sect. 4. Both anthropogenic and biomass burning emissions are seen in SEA inventories. The peak was observed in MAM, although only a few observations were available for JJA owing to the high cloud occurrences.

### 10 3.2 Comparison of the GOSAT and IASI L2 product

Results from the GOSAT are compared with the IASI ammonia product. Similar to Figure 3, the columnar ammonia concentrations over land obtained from the IASI are shown in Figure 7. The time period of observation was the same as for the GOSAT data and spanned from 23 April 2009 to 14 December 2014. The data are filtered for only daytime and no clouds. The horizontal distributions and seasonal variations observed for the GOSAT and IASI data in Figure 3 and Figure 7 show similar patterns. Nonetheless, some differences were noted. The differences between Figure 3 and Figure 7 are shown in Figure 8. As a whole, the values from the GOSAT tend to be larger than those from the IASI. The differences were especially large in several areas. The values from the GOSAT were much higher than those from the IASI in such as Western Africa and Southern India during JJA. On the other hand, they were smaller in the coastal area of central Africa during DJF, in Northern India during JJA, and in Eastern China during JJA. These differences are discussed in the next section.

The time series of the monthly averaged columnar ammonia concentrations, obtained from the GOSAT and IASI for the six agricultural emission areas (CUS, EUR, CAS, IND, SEA, and ECH) outlined in Table 2, are shown in Figure 9. In IND, SEA, and ECH, the peak term was short (i.e., one or two months). On the other hand, in CUS, EUR, and CAS, the peak terms were relatively long, about three or four months. The temporal variation patterns in the values obtained from the GOSAT and IASI were similar, although some differences in the magnitude were noted as per the results shown in Figure 8. In the CUS, the values from the GOSAT and IASI were in good agreement. With the exception of 2010, the GOSAT estimated higher values in the peak season over EUR. A similar trend was noted for both CAS and SEA. The differences were especially large for CAS. Although the peak values were not so different for IND and ECH, the GOSAT values in the bottoms were higher. Figure 10 is similar to Figure 9, but for the biomass burning areas (SAM, CAF, SAF, and WRU). The variations of peak value between each year over SAM were larger than those over the other areas. In contrast, the peak values in SAF were very similar across the years. This should be reflected in the difference in scale of biomass burning among the years. For example, only the value of August 2010 for WRU was quite large, which is attributed to the large-scale wildfires that occurred during this period. The consistency between the results from the GOSAT and IASI in these areas is higher than that observed in Figure 9. However, the largest difference was observed over CAF. Although the IASI shows peaks around March, the peak for the GOSAT



appeared in summer and the values from March were much smaller than those from the IASI. One of the causes for these high summer values from the GOSAT is probably dust aerosol contamination, as discussed in Sect. 4.

The monthly mean  $2.5^\circ \times 2.5^\circ$  grid scatter plots between the GOSAT and IASI in the agricultural and biomass burning source areas are shown in Figure 11 and Figure 12, respectively. The slopes tend to be lower than 1, which is due to the GOSAT values being higher at lower concentrations, as seen in the previous figures. The correlation coefficients for IND (0.79) and SEA (0.77) were relatively high. On the other hand, they were relatively low for CUS, EUR, and ECH, where vast application of nitrogen fertilizers has been reported (Potter et al., 2010; Lu and Tian, 2017). Despite some biases, the slopes for both CAS and SAF were close to 1. In the biomass burning areas, the correlation coefficients were similar.

## 10 4 Discussion

The comparison between the GOSAT and IASI product results showed a similarity in the spatial and temporal distributions. However, some differences larger than the level of estimated errors shown in Figure 4 were also found as noted in the previous section. The possible main causes generating differences are (1) scan geometry, (2) local time of observation, (3) spectral resolution, (4) signal to noise ratio, (5) assumed ammonia profile, and (6) cloud/aerosol screening. In the previous section, the differences between the values from the GOSAT and IASI were relatively large above agricultural areas, as shown in Figure 8, Figure 9, and Figure 11. The temporal gap of (2) is probably to incur the most significant differences in the measured values because the anthropogenic ammonia emissions should be temporally variable. There is about 3.5 h gap between the GOSAT and IASI observations. Several studies have investigated the diurnal variations in atmospheric ammonia concentrations near the surface. According to these studies, the variations are especially large over agricultural areas during the summer season, with patterns differing for each location (e.g., Erismann et al., 2001, Meng et al., 2011, Sharma et al., 2014, Wang et al., 2015). These reports estimated that the variations fluctuate along with the temporal variations in human activities, such as fertilization and traffic. Therefore, one of the largest causes for the differences between the GOSAT and IASI in agricultural areas, such as India and China, is likely the temporal variation. The other possible cause is (5) in these areas. In this study, the ammonia profile shape is assumed to be that of the AFGL profiles. However, the vertical gradient of the concentration can be much larger in source regions. The GOSAT retrieval has a sensitivity in the middle troposphere as mentioned in Sect. 2, and therefore the scaled profile from the GOSAT retrieval likely underestimates the concentrations near the surface in these situations. On the other hand, the IASI retrieval uses the a priori profiles from the model calculations and the vertical gradient is more realistic. As a result, the column integrated values from the GOSAT are lower in agricultural source areas, such as CUS, IND, and ECH where the lower values from GOSAT are seen in Figure 8 during the peak season. Over smaller and more scattered agricultural areas as compared to hotspots, such as those noted for EUR, (1) likely also contributes to the differences noted in Figure 9.

In addition, the sensitivity of the TIR measurements changes diurnally because of the diurnal thermal contrast between surface skin and air. In many cases, the surface temperature at the GOSAT measurement time is higher than that at the IASI



measurement time during the daytime. As a result, the thermal contrast was larger at the GOSAT measurement. Clarisse et al. (2010) compared ammonia retrievals using both the IASI and the TES, which have observation times close to that of the GOSAT and a higher spectral resolution than that of the IASI. They reported that the thermal contrast was larger, the spectral resolution was higher, and the sensitivity to the lower level was higher. Therefore, the GOSAT should be more sensitive to the lower atmospheric levels where, in many cases, the concentration of ammonia is generally higher than that in the high levels as compared to the IASI. Therefore, it is likely that this effect is dominant for the low concentrations as seen in Figure 11 and Figure 12.

In Figure 8 and Figure 10, the largest differences were observed over CAF. The time series from the GOSAT has two peaks around March and July. The peaks in March are consistent with those observed by Whitburn et al. (2015), who reported that these peaks, observed from the IASI product, were related to biomass burning at the end of the boreal winter in this area. Part of those peaks observed in July from the GOSAT, particularly the high values in Northwestern Africa during JJA (Figure 8), are probably influenced by dust aerosols. The presence of dust can lead to the overestimation of ammonia because of the wavenumber dependence of its absorption properties. Figure 13 shows an example of the observed spectra contaminated by dust aerosols over Saharan desert. The residual shows some similarity of wavenumber dependencies of ammonia signals on the spectra. Since it is very hard to detect dust aerosols over desert surfaces using only a visible imager, in this study, the dusty scenes were eliminated by the CO<sub>2</sub> slicing technique that uses the TIR region in addition to CAI cloud screening. If CO<sub>2</sub> slicing is not used for the screening, high apparent ammonia concentrations are calculated over the Saharan desert in JJA, where no emission sources are present, as a result of the frequent dust storms that occur in this region. However, the dusty scenes are not completely eliminated by this technique. Therefore, the high concentrations observed over Western Sahara during JJA (Figure 3) probably reflect a degree of dust contamination. On the other hand, the high values obtained by the GOSAT over CAF in the boreal spring and summer may not only result from dust contamination. The seasonal variations observed by AIRS and reported by Warner et al. (2016) showed similarly high concentrations in central Africa during MAM and JJA. This area is characterized by a number of distributed surface types whose temporal patterns of ammonia concentrations are different for each. Figure 14 shows the monthly variations in ammonia concentrations over six surface types, derived from GOSAT. Peaks over forests or woody savannas were observed in February or March, similar to the IASI observations. In contrast, peaks were noted in the boreal summer over open shrublands, grasslands, and croplands. Adon et al. (2010) reported that the peaks in atmospheric ammonia concentrations are more commonly detected during the wet season (boreal summer) over dry savannas, whereas those detected during the dry season (boreal winter) were found over wet savannas and forests. Herein, grasslands are included in the dry savanna categorization as per Adon et al. (2010), and the observed patterns in Figure 14 are consistent with this report. Therefore, the peaks in the boreal summer observed by the GOSAT might be a result of the high concentrations over surfaces such as grasslands and open shrublands. Further studies are required to investigate the source, sink, and concentration patterns and to understand the dynamics of ammonia in this area.



## 5 Summary

Columnar ammonia concentrations were retrieved using the thermal infrared spectra obtained from the GOSAT for a period of approximately five years. The optimal estimation, which iteratively decreases the difference between the calculated and the observed spectra, was used for analysis. Temperature and water vapor profiles were also retrieved sequentially in order to reduce retrieval errors. The gridded horizontal distributions of atmospheric columnar ammonia concentrations for each season (DJF, MAM, JJA, and SON) were shown. Significantly high concentrations were noted in central US, South America, Europe, Central Africa, South Africa, Western Russia, Central Asia, India, Southeast Asia, and Eastern China. These distributions are similar to those previously reported using the other sounders. The areas categorized as anthropogenic and biomass burning emission source regions, based on inventories and characteristics, were investigated. The hotspots noted in the data were consistent with those from the inventories. However, high values were detected in Central Asia in spite of the lower inventoried emissions. These high values likely resulted from the application of fertilizers for cotton production, as reported by in situ observations. The regional time series of the concentrations in those areas clearly detect the high and low seasons. A comparison with the IASI ammonia product showed a good agreement horizontally and temporally, although there were some differences in the details. The values obtained from the GOSAT data tend to be large relative to the background level of concentrations in the spring and summer. Differences are especially large in areas and during seasons with heavy fertilizer application. It seems that the largest causes of these differences are the temporal gaps in the observations due to diurnal variations in ammonia emissions and the thermal contrast between surface skin and air. In the biomass burning emission areas, the consistency is relatively high. The largest differences were noted in Central Africa. These differences may stem from dust contamination and the variation in seasonal patterns over various surface types.

In a recent paper, it was reported that the use of nitrogen fertilizers has been increasing (Lu and Tian, 2017) and that this trend will continue with the growth of the human population. Hence, it is urgent to continue monitoring global atmospheric ammonia in order to understand its influence on the environment. The same analysis will be applicable to data from GOSAT-2, which was launched in October 2018. This will lead to the construction of a long-term ammonia database. In addition, GOSAT-2 will be able to observe CO<sub>2</sub>, CH<sub>4</sub>, and CO simultaneously with ammonia. This combination of observed products is useful for better understanding the role of specific phenomena, such as biomass burning and agricultural activities.

## Acknowledgements

This work was supported by JSPS KAKENHI Grant number 17K17670 and the program of JAXA (JX-PSPC-455165). The computational resources were partly provided by NIES-RCF2.



## References

- Aardenne, J. A. van, Dentener, F. J., Olivier, J. G. J., Goldewijk, C. G. M. and Lelieveld, J.: A  $1 \times 1$  resolution data set of historical anthropogenic trace gas emissions for the period 1890–1990, *Global Biogeochem. Cycles*, 15(4), 909–928, 2001.
- Adon, M., Galy-Lacaux, C., Yoboué, V., Delon, C., Lacaux, J. P., Castera, P., Gardrat, E., Pienaar, J., Ourabi, H. Al and  
5 Laouali, D.: Long term measurements of sulfur dioxide, nitrogen dioxide, ammonia, nitric acid and ozone in Africa using passive samplers, *Atmos. Chem. Phys.*, 10(15), 7467–7487, 2010.
- Akagi, S. K., Yokelson, R. J., Wiedinmyer, C., Alvarado, M. J., Reid, J. S., Karl, T., Crouse, J. D. and Wennberg, P. O.: Emission factors for open and domestic biomass burning for use in atmospheric models, *Atmos. Chem. Phys.*, 11(9), 4039–4072, 2011.
- 10 Anderson, G. P., Clough, S. A., Kneizys, F. X., Chetwynd, J. H. and Shettle, E. P.: AFGL Atmospheric Constituent Profiles (0.120km), 1986.
- Baldrige, A. M., Hook, S. J., Grove, C. I. and Rivera, G.: The ASTER spectral library version 2.0, *Remote Sens. Environ.*, 113(4), 711–715, doi:10.1016/j.rse.2008.11.007, 2009.
- Beer, R., Shephard, M. W., Kulawik, S. S., Clough, S. A., Eldering, A., Bowman, K. W., Sander, S. P., Fisher, B. M., Payne,  
15 V. H. and Luo, M.: First satellite observations of lower tropospheric ammonia and methanol, *Geophys. Res. Lett.*, 35(9), 2008.
- Behera, S. N., Sharma, M., Aneja, V. P. and Balasubramanian, R.: Ammonia in the atmosphere: a review on emission sources, atmospheric chemistry and deposition on terrestrial bodies, *Environ. Sci. Pollut. Res.*, 20(11), 8092–8131, 2013.
- Clarisse, L., Clerbaux, C., Dentener, F., Hurtmans, D. and Coheur, P.-F.: Global ammonia distribution derived from infrared  
20 satellite observations, *Nat. Geosci.*, 2(7), 479–483, 2009.
- Clarisse, L., Shephard, M. W., Dentener, F., Hurtmans, D., Cady-Pereira, K., Karagulian, F., Van Damme, M., Clerbaux, C. and Coheur, P.: Satellite monitoring of ammonia: A case study of the San Joaquin Valley, *J. Geophys. Res. Atmos.*, 115(D13), 2010.
- Clough, S. A., Shephard, M. W., Mlawer, E., Delamere, J. S., Iacono, M., Cady-Pereira, K., Boukabara, S. and Brown, P. D.:  
25 Atmospheric radiative transfer modeling: a summary of the AER codes, *J. Quant. Spectrosc. Radiat. Transf.*, 91(2), 233–244, doi:10.1016/j.jqsrt.2004.05.058, 2005.
- Van Damme, M., Clarisse, L., Heald, C. L., Hurtmans, D., Ngadi, Y., Clerbaux, C., Dolman, A. J., Erisman, J. W. and Coheur, P.-F.: Global distributions, time series and error characterization of atmospheric ammonia (NH<sub>3</sub>) from IASI satellite observations, *Atmos. Chem. Phys.*, 14(6), 2905–2922, 2014.
- 30 Van Damme, M., Erisman, J. W., Clarisse, L., Dammers, E., Whitburn, S., Clerbaux, C., Dolman, A. J. and Coheur, P.: Worldwide spatiotemporal atmospheric ammonia (NH<sub>3</sub>) columns variability revealed by satellite, *Geophys. Res. Lett.*, 42(20), 8660–8668, 2015.



- Van Damme, M., Whitburn, S., Clarisse, L., Clerbaux, C., Hurtmans, D. and Coheur, P. F.: Version 2 of the IASI NH<sub>3</sub> neural network retrieval algorithm: near-real-time and reanalysed datasets, *Atmos. Meas. Tech.*, 10(12), 4905–4914, doi:10.5194/amt-10-4905-2017, 2017.
- Dammers, E., Palm, M., Van Damme, M., Vigouroux, C., Smale, D., Conway, S., Toon, G. C., Jones, N., Nussbaumer, E.,  
5 Warneke, T., Petri, C., Clarisse, L., Clerbaux, C., Hermans, C., Lutsch, E., Strong, K., Hannigan, J. W., Nakajima, H.,  
Morino, I., Herrera, B., Stremme, W., Grutter, M., Schaap, M., Wichink Kruit, R. J., Notholt, J., Coheur, P. F. and Erisman,  
J. W.: An evaluation of IASI-NH<sub>3</sub> with ground-based Fourier transform infrared spectroscopy measurements, *Atmos. Chem.  
Phys.*, 16(16), 10351–10368, doi:10.5194/acp-16-10351-2016, 2016.
- Erisman, J. W., Otjes, R., Hensen, A., Jongejan, P., van den Bulk, P., Khlystov, A., Möls, H. and Slanina, S.: Instrument  
10 development and application in studies and monitoring of ambient ammonia, *Atmos. Environ.*, 35(11), 1913–1922, 2001.
- Friedl, M. A., Sulla-Menashe, D., Tan, B., Schneider, A., Ramankutty, N., Sibley, A. and Huang, X.: MODIS Collection 5  
global land cover: Algorithm refinements and characterization of new datasets, *Remote Sens. Environ.*, 114(1), 168–182,  
2010.
- Galloway, J. N., Dentener, F. J., Capone, D. G., Boyer, E. W., Howarth, R. W., Seitzinger, S. P., Asner, G. P., Cleveland, C.  
15 C., Green, P. A. and Holland, E. A.: Nitrogen cycles: past, present, and future, *Biogeochemistry*, 70(2), 153–226, 2004.
- Giglio, L., Randerson, J. T. and Werf, G. R.: Analysis of daily, monthly, and annual burned area using the fourth-generation  
global fire emissions database (GFED4), *J. Geophys. Res. Biogeosciences*, 118(1), 317–328, 2013.
- Huang, X., Song, Y., Li, M., Li, J., Huo, Q., Cai, X., Zhu, T., Hu, M. and Zhang, H.: A high-resolution ammonia emission  
inventory in China, *Global Biogeochem. Cycles*, 26(1), 2012.
- 20 Ishida, H. and Nakajima, T. Y.: Development of an unbiased cloud detection algorithm for a spaceborne multispectral  
imager, *J. Geophys. Res.*, 114, doi:10.1029/2008jd010710, 2009.
- Janssens-Maenhout, G., Dentener, F., Van Aardenne, J., Monni, S., Pagliari, V., Orlandini, L., Klimont, Z., Kurokawa, J.,  
Akimoto, H. and Ohara, T.: EDGAR-HTAP: a harmonized gridded air pollution emission dataset based on national  
inventories, *Eur. Comm. Jt. Res. Cent. Inst. Environ. Sustain. JRC 68434 UR 25229 EUR 25229*, ISBN 978-92-79-23123-0,  
25 2012.
- Kataoka, F., Knuteson, R. O., Kuze, A., Suto, H., Shiomi, K., Harada, M., Garms, E. M., Roman, J. A., Tobin, D. C., Taylor,  
J. K., Revercomb, T. H., Sekio, N., Higuchi, R. and Mitomi, Y.: TIR Spectral Radiance Calibration of the GOSAT Satellite  
Borne TANSO-FTS With the Aircraft-Based S-HIS and the Ground-Based S-AERI at the Railroad Valley Desert Playa,  
*IEEE Trans. Geosci. Remote Sens.*, 52(1), 89–105, doi:10.1109/TGRS.2012.2236561, 2013.
- 30 Kuze, A., Suto, H., Nakajima, M. and Hamazaki, T.: Thermal and near infrared sensor for carbon observation Fourier-  
transform spectrometer on the Greenhouse Gases Observing Satellite for greenhouse gases monitoring, *Appl. Opt.*, 48(35),  
6716–6733, doi:10.1364/ao.48.006716, 2009.



- Kuze, A., Suto, H., Shiomi, K., Urabe, T., Nakajima, M., Yoshida, J., Kawashima, T., Yamamoto, Y., Kataoka, F. and Buijs, H.: Level 1 algorithms for TANSO on GOSAT: processing and on-orbit calibrations, *Atmos. Meas. Tech.*, 5(10), 2447–2467, doi:10.5194/amt-5-2447-2012, 2012.
- Kuze, A., Suto, H., Shiomi, K., Kawakami, S., Tanaka, M., Ueda, Y., Deguchi, A., Yoshida, J., Yamamoto, Y., Kataoka, F., Taylor, T. E. and Buijs, H. L.: Update on GOSAT TANSO-FTS performance, operations, and data products after more than 6 years in space, *Atmos. Meas. Tech.*, 9(6), 2445–2461, doi:10.5194/amt-9-2445-2016, 2016.
- Li, K. H., Song, W., Liu, X. J., Shen, J. L., Luo, X. S., Sui, X. Q., Liu, B., Hu, Y. K., Christie, P. and Tian, C. Y.: Atmospheric reactive nitrogen concentrations at ten sites with contrasting land use in an arid region of central Asia, *Biogeosciences*, 9(10), 4013–4021, doi:10.5194/bg-9-4013-2012, 2012.
- Lu, C. and Tian, H.: Global nitrogen and phosphorus fertilizer use for agriculture production in the past half century: shifted hot spots and nutrient imbalance, *Earth Syst. Sci. Data*, 9(1), 181–192, doi:10.5194/essd-9-181-2017, 2017.
- Meng, Z. Y., Lin, W. L., Jiang, X. M., Yan, P., Wang, Y., Zhang, Y. M., Jia, X. F. and Yu, X. L.: Characteristics of atmospheric ammonia over Beijing, China, *Atmos. Chem. Phys.*, 11(12), 6139–6151, doi:10.5194/acp-11-6139-2011, 2011.
- Potter, P., Ramankutty, N., Bennett, E. M. and Donner, S. D.: Characterizing the Spatial Patterns of Global Fertilizer Application and Manure Production, *Earth Interact.*, 14(2), 1–22, doi:10.1175/2009ei288.1, 2010.
- Randerson J.T., G. R. van der W. L. G. G. J. C. and Kasibhatla, P. S.: Global Fire Emissions Database, Version 4.1 (GFEDv4), 2017.
- Rodgers, C. D.: Inverse methods for atmospheric sounding: theory and practice, World scientific., 2000.
- Rothman, L. S., Gordon, I. E., Babikov, Y., Barbe, A., Chris Benner, D., Bernath, P. F., Birk, M., Bizzocchi, L., Boudon, V., Brown, L. R., Campargue, A., Chance, K., Cohen, E. A., Coudert, L. H., Devi, V. M., Drouin, B. J., Fayt, A., Flaud, J.-M., Gamache, R. R., Harrison, J. J., Hartmann, J.-M., Hill, C., Hodges, J. T., Jacquemart, D., Jolly, A., Lamouroux, J., Le Roy, R. J., Li, G., Long, D. A., Lyulin, O. M., Mackie, C. J., Massie, S. T., Mikhailenko, S., Müller, H. S. P., Naumenko, O. V., Nikitin, A. V., Orphal, J., Perevalov, V., Perrin, A., Polovtseva, E. R., Richard, C., Smith, M. A. H., Starikova, E., Sung, K., Tashkun, S., Tennyson, J., Toon, G. C., Tyuterev, V. G. and Wagner, G.: The HITRAN2012 molecular spectroscopic database, *J. Quant. Spectrosc. Radiat. Transf.*, 130, 4–50, doi:10.1016/J.JQSRT.2013.07.002, 2013.
- Saeki, T., Saito, R., Belikov, D. and Maksyutov, S.: Global high-resolution simulations of CO<sub>2</sub> and CH<sub>4</sub> using a NIES transport model to produce a priori concentrations for use in satellite data retrievals, *Geosci. Model Dev.*, 6(1), 81–100, 2013.
- Saitoh, N., Imasu, R., Ota, Y. and Niwa, Y.: CO<sub>2</sub> retrieval algorithm for the thermal infrared spectra of the Greenhouse Gases Observing Satellite: Potential of retrieving CO<sub>2</sub> vertical profile from high-resolution FTS sensor, *J. Geophys. Res.*, 114, doi:10.1029/2008jd011500, 2009.
- Saitoh, N., Kimoto, S., Sugimura, R., Imasu, R., Kawakami, S., Shiomi, K., Kuze, A., Machida, T., Sawa, Y. and Matsueda, H.: Algorithm update of the GOSAT/TANSO-FTS thermal infrared CO<sub>2</sub> product (version 1) and validation of the UTLS CO<sub>2</sub> data using CONTRAIL measurements, *Atmos. Meas. Tech.*, 9(5), 2119–2134, doi:10.5194/amt-9-2119-2016, 2016.



- Seinfeld, J. H. and Pandis, S. N.: Atmospheric chemistry and physics: from air pollution to climate change, John Wiley & Sons., 2016.
- Sharma, S. K., Kumar, M., Rohtash, Gupta, N. C., Saraswati, Saxena, M. and Mandal, T. K.: Characteristics of ambient ammonia over Delhi, India, *Meteorol. Atmos. Phys.*, 124(1), 67–82, doi:10.1007/s00703-013-0299-8, 2014.
- 5 Shephard, M. W. and Cady-Pereira, K. E.: Cross-track Infrared Sounder (CrIS) satellite observations of tropospheric ammonia, *Atmos. Meas. Tech.*, 8(3), 1323–1336, doi:10.5194/amt-8-1323-2015, 2015.
- Shephard, M. W., Cady-Pereira, K. E., Luo, M., Henze, D. K., Pinder, R. W., Walker, J. T., Rinsland, C. P., Bash, J. O., Zhu, L. and Payne, V. H.: TES ammonia retrieval strategy and global observations of the spatial and seasonal variability of ammonia, *Atmos. Chem. Phys.*, 11(20), 10743–10763, 2011.
- 10 Someya, Y., Imasu, R., Saitoh, N., Ota, Y. and Shiomi, K.: A development of cloud top height retrieval using thermal infrared spectra observed with GOSAT and comparison with CALIPSO data, *Atmos. Meas. Tech.*, 9(5), doi:10.5194/amt-9-1981-2016, 2016.
- Wang, S., Nan, J., Shi, C., Fu, Q., Gao, S., Wang, D., Cui, H., Saiz-Lopez, A. and Zhou, B.: Atmospheric ammonia and its impacts on regional air quality over the megacity of Shanghai, China, *Sci. Rep.*, 5, 2015.
- 15 Warner, J. X., Wei, Z., Strow, L. L., Dickerson, R. R. and Nowak, J. B.: The global tropospheric ammonia distribution as seen in the 13-year AIRS measurement record, *Atmos. Chem. Phys.*, 16(8), 5467–5479, doi:10.5194/acp-16-5467-2016, 2016.
- Warner, J. X., Dickerson, R. R., Wei, Z., Strow, L. L., Wang, Y. and Liang, Q.: Increased atmospheric ammonia over the world's major agricultural areas detected from space, *Geophys. Res. Lett.*, 44(6), 2875–2884, 2017.
- 20 Whitburn, S., Van Damme, M., Kaiser, J. W., Van Der Werf, G. R., Turquety, S., Hurtmans, D., Clarisse, L., Clerbaux, C. and Coheur, P.-F.: Ammonia emissions in tropical biomass burning regions: Comparison between satellite-derived emissions and bottom-up fire inventories, *Atmos. Environ.*, 121, 42–54, 2015.
- Yoshida, Y., Ota, Y., Eguchi, N., Kikuchi, N., Nobuta, K., Tran, H., Morino, I. and Yokota, T.: Retrieval algorithm for CO<sub>2</sub> and CH<sub>4</sub> column abundances from short-wavelength infrared spectral observations by the Greenhouse gases observing  
25 satellite, *Atmos. Meas. Tech.*, 4(4), 717–734, doi:10.5194/amt-4-717-2011, 2011.
- Yoshida, Y., Kikuchi, N., Morino, I., Uchino, O., Oshchepkov, S., Bril, A., Saeki, T., Schutgens, N., Toon, G. C., Wunch, D., Roehl, C. M., Wennberg, P. O., Griffith, D. W. T., Deutscher, N. M., Warneke, T., Notholt, J., Robinson, J., Sherlock, V., Connor, B., Rettinger, M., Sussmann, R., Ahonen, P., Heikkinen, P., Kyro, E., Mendonca, J., Strong, K., Hase, F., Dohe, S. and Yokota, T.: Improvement of the retrieval algorithm for GOSAT SWIR XCO<sub>2</sub> and XCH<sub>4</sub> and their validation using  
30 TCCON data, *Atmos. Meas. Tech.*, 6(6), 1533–1547, doi:10.5194/amt-6-1533-2013, 2013.

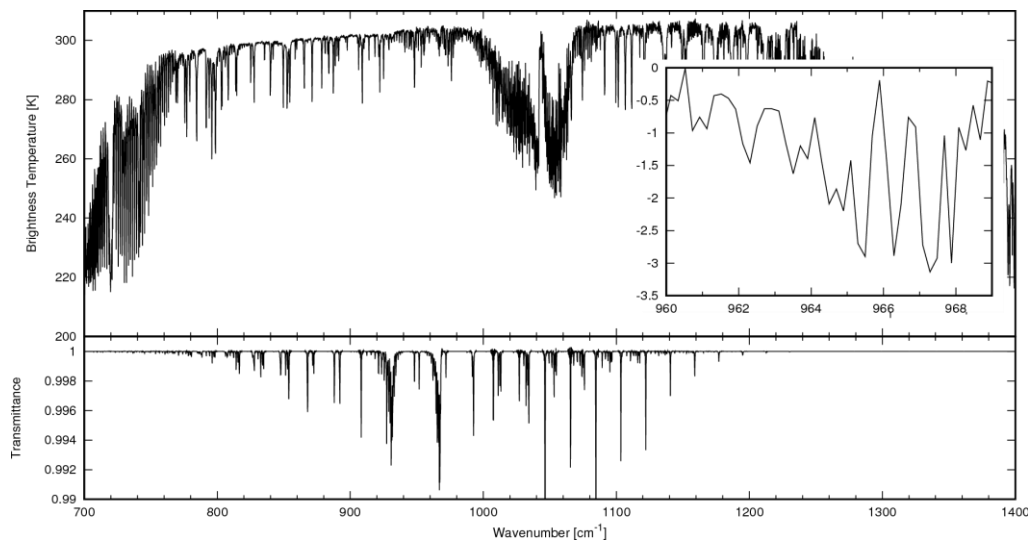


**Figure 1:** Observed spectra by the GOSAT at (75.85°E, 29.80°N) on 15 July 2013 (top), the residuals between the observed spectra and the one calculated without NH<sub>3</sub> (right inside), and NH<sub>3</sub> transmittance using the AFGL profile (bottom).

5

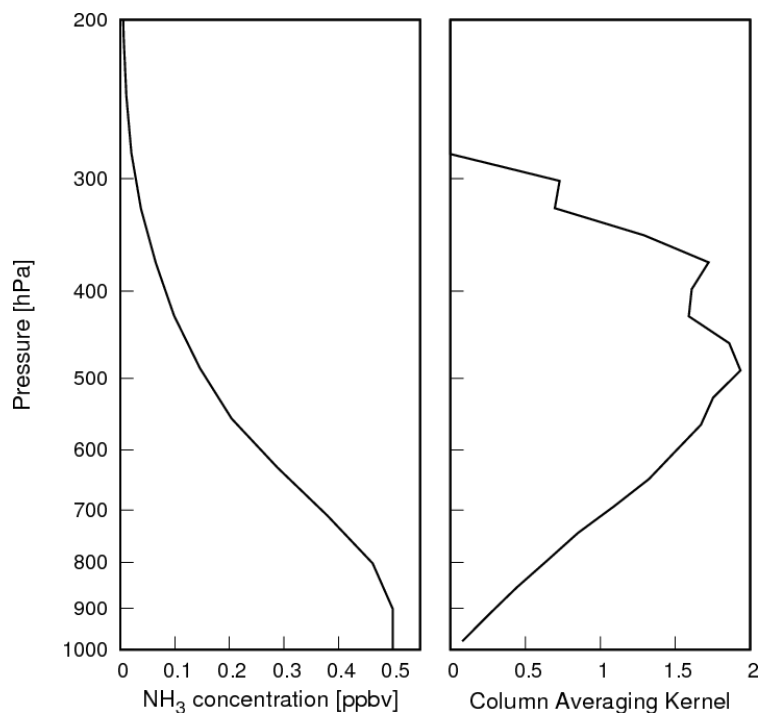


**Figure 2:** Ammonia concentration of the AFGL profiles (left) and the column averaging kernel for the a priori ammonia profile using mid-latitude summer atmosphere (right).



**Table 1:** Wavenumber range and a priori information used in the retrieval steps.

Retrieved parameter	Wavenumber range ( $\text{cm}^{-1}$ )	A priori
Temperature	720–780	GPV (GSM)
Water vapor	1,205–1,245	GPV (GSM)
Ammonia profile	960–969	AFGL profile

5

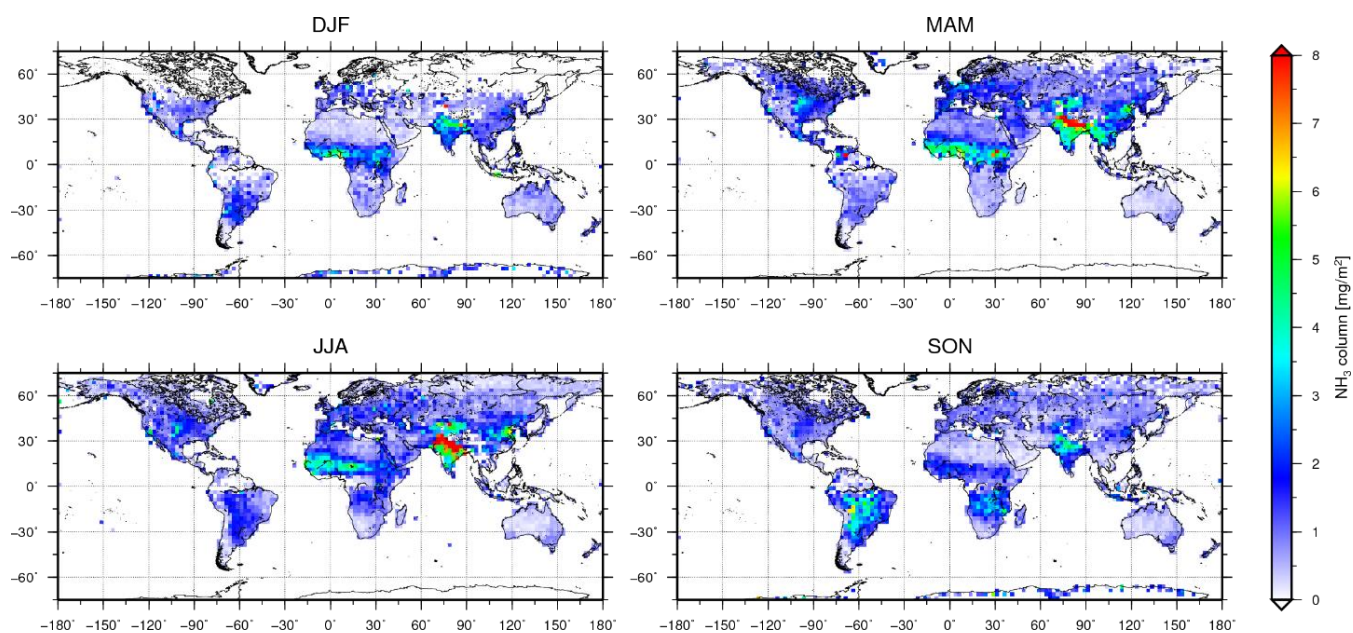


**Figure 3:** Horizontal distributions of columnar ammonia concentrations for each season (December to February, DJF; March to May, MAM; June to August, JJA; September to November, SON) retrieved from the GOSAT over  $2.5^\circ \times 2.5^\circ$  grids averaged from April 2009 to May 2014.

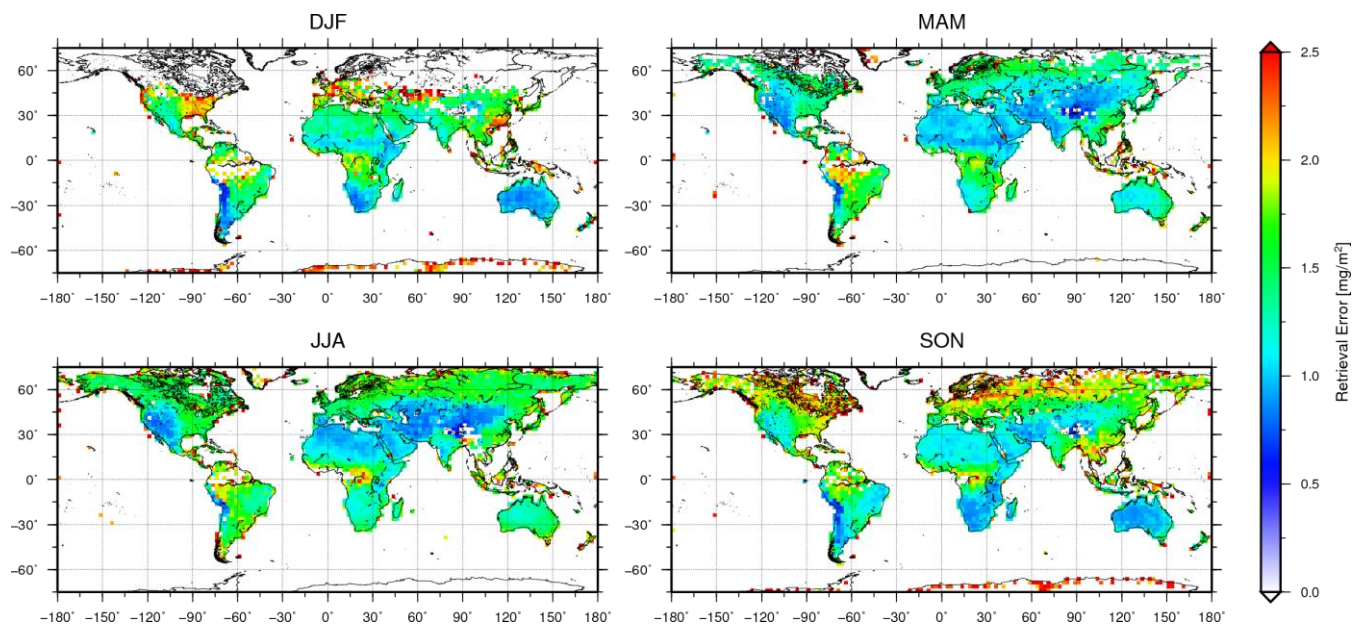


Figure 4 Same as Figure 3 but for averaged errors.

5

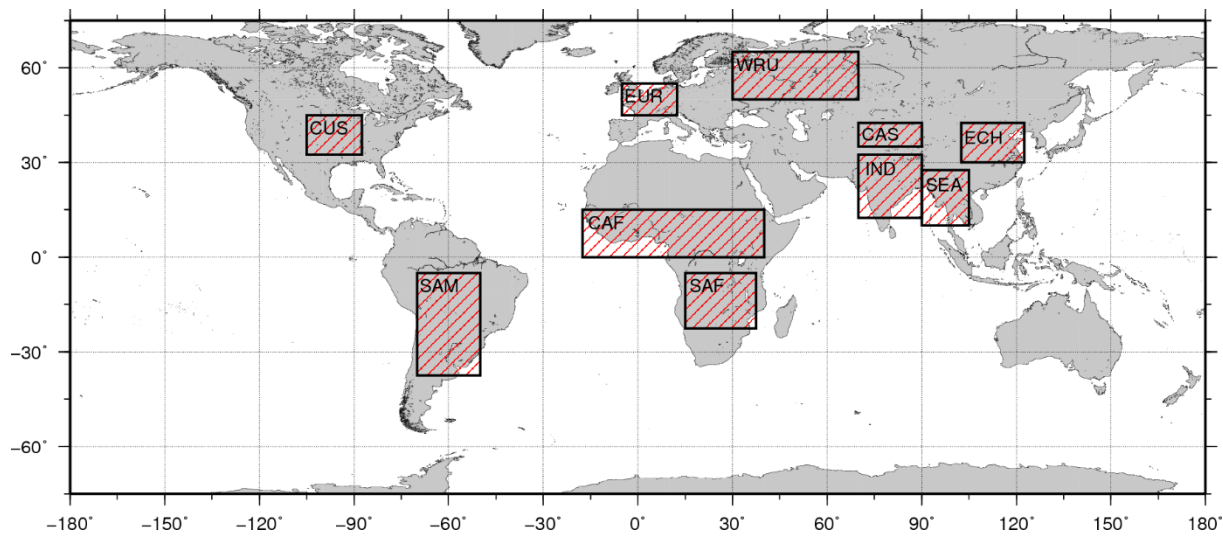
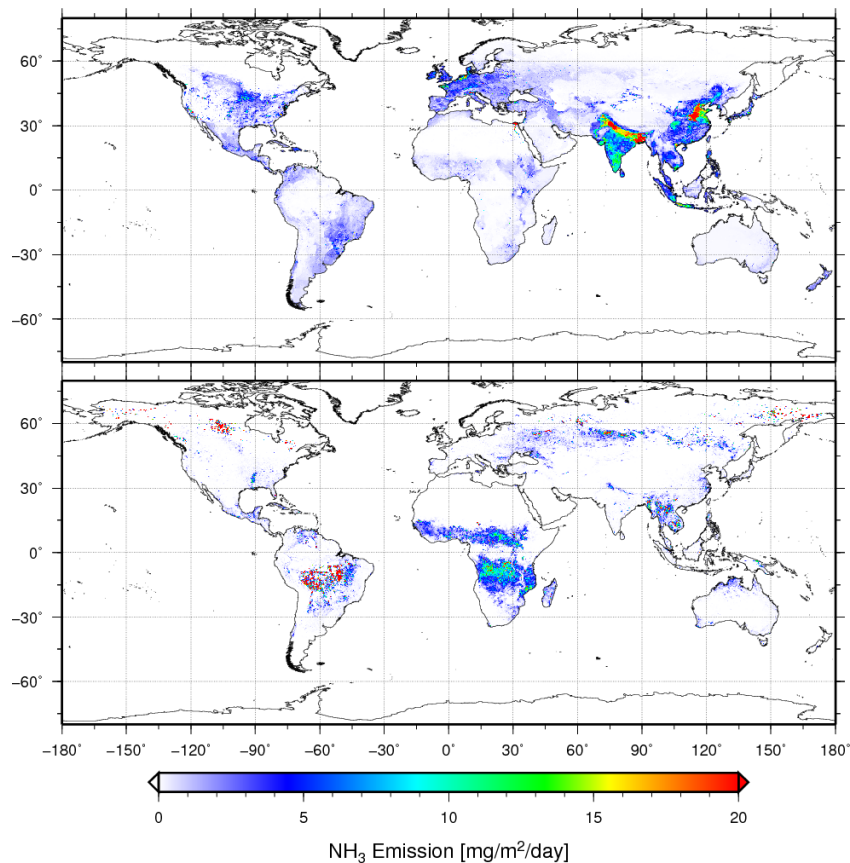


Figure 5: Distribution of areas with high ammonia concentrations obtained from the GOSAT.



**Table 2:** List of areas indicated in Figure 5 and their locations.

Area	Location
Central US (CUS)	(32.5°N–45°N, 105°W–87.5°W)
South America (SAM)	(37.5°S–5°S, 70°W–50°W)
Europe (EUR)	(45°N–55°N, 5°W–12.5°E)
Central Africa (CAF)	(0°–15°N, 17.5°W–40°E)
South Africa (SAF)	(22.5°S–5°S, 15°E–37.5°E)
Western Russia (WRU)	(50°N–65°N, 30°E–70°E)
Central Asia (CAS)	(35°N–42.5°N, 70°E–90°E)
India (IND)	(12.5°N–32.5°N, 70°E–90°E)
Southeast Asia (SEA)	(10°N–27.5°N, 90°E–105°E)
Eastern China (ECH)	(30°N–42.5°N, 102.5°E–122.5°E)



**Figure 6:** Anthropogenic ammonia emissions in 2010 obtained from EDGAR-HTAP v2 (top) and the biomass burning emissions from GFED4.1s (bottom).

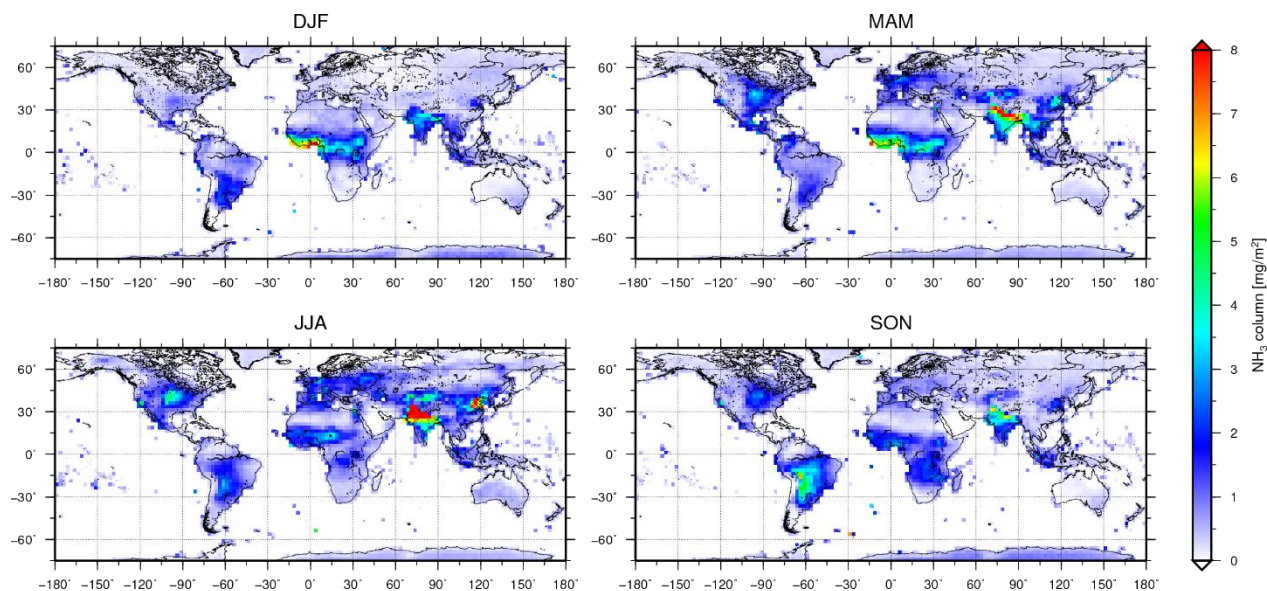
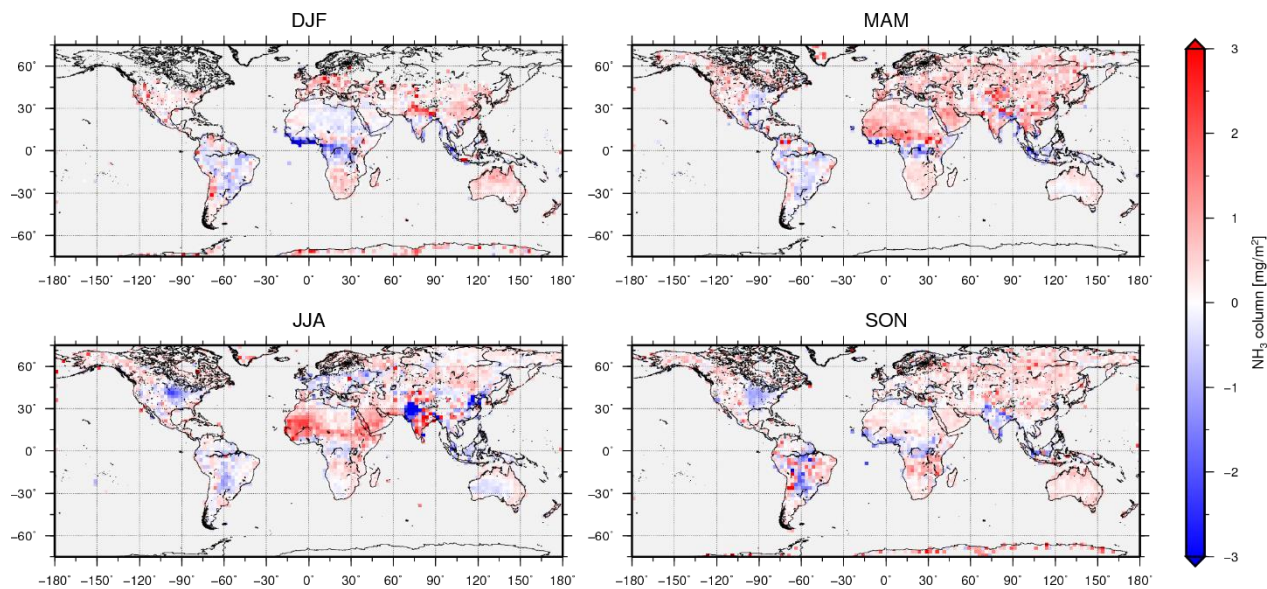
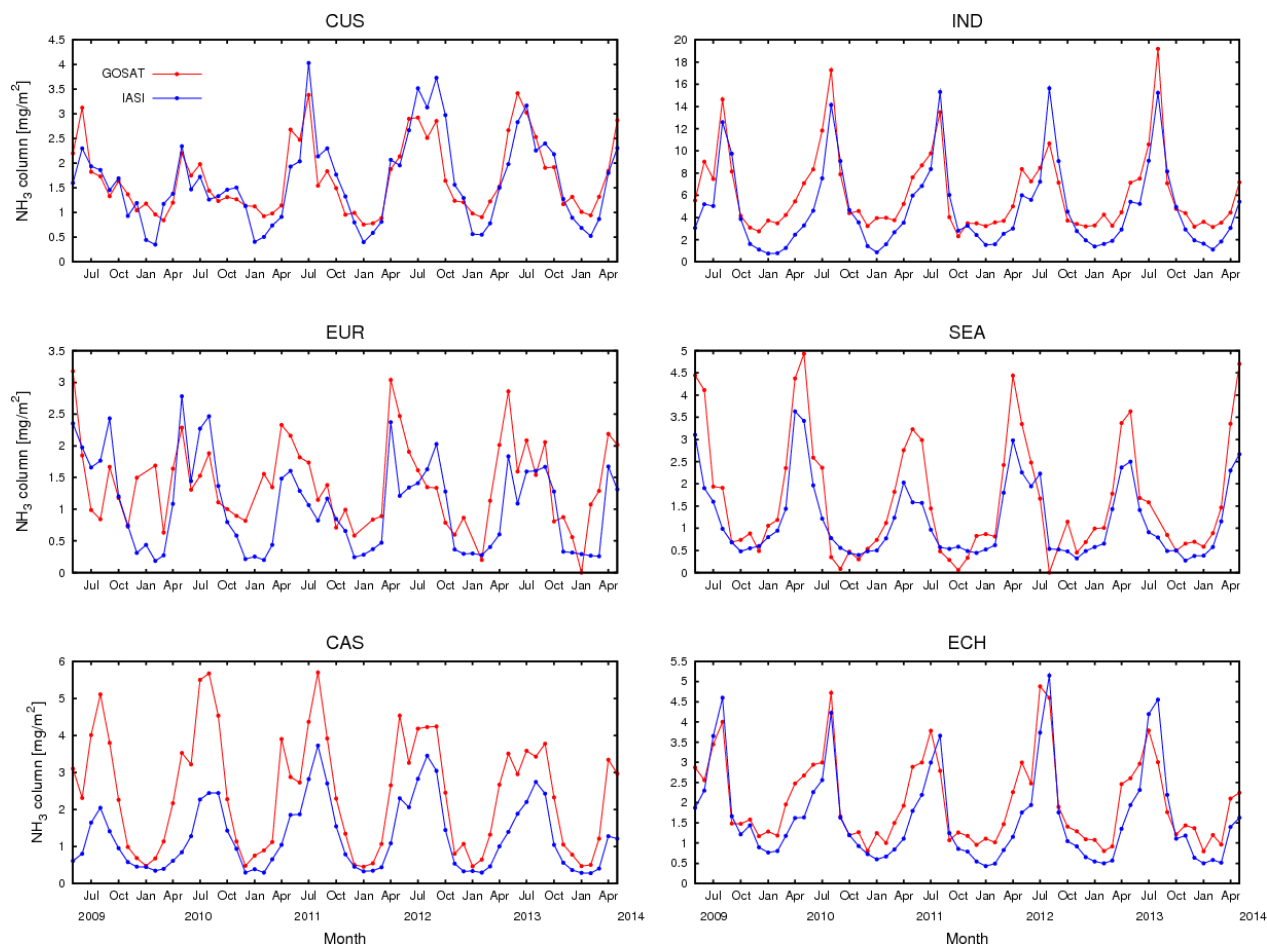


Figure 7: Same as Figure 3, but for the IASI measurements.



5 Figure 8: Same as Figure 3, but for the difference between the GOSAT and the IASI columnar ammonia concentrations. The red color indicates that the GOSAT data is higher than that from the IASI.



**Figure 9:** Time series of the monthly averaged columnar ammonia concentrations from the GOSAT (red) and IASI (blue) from May 2009 to May 2014 in the agricultural emission areas noted in Table 2.

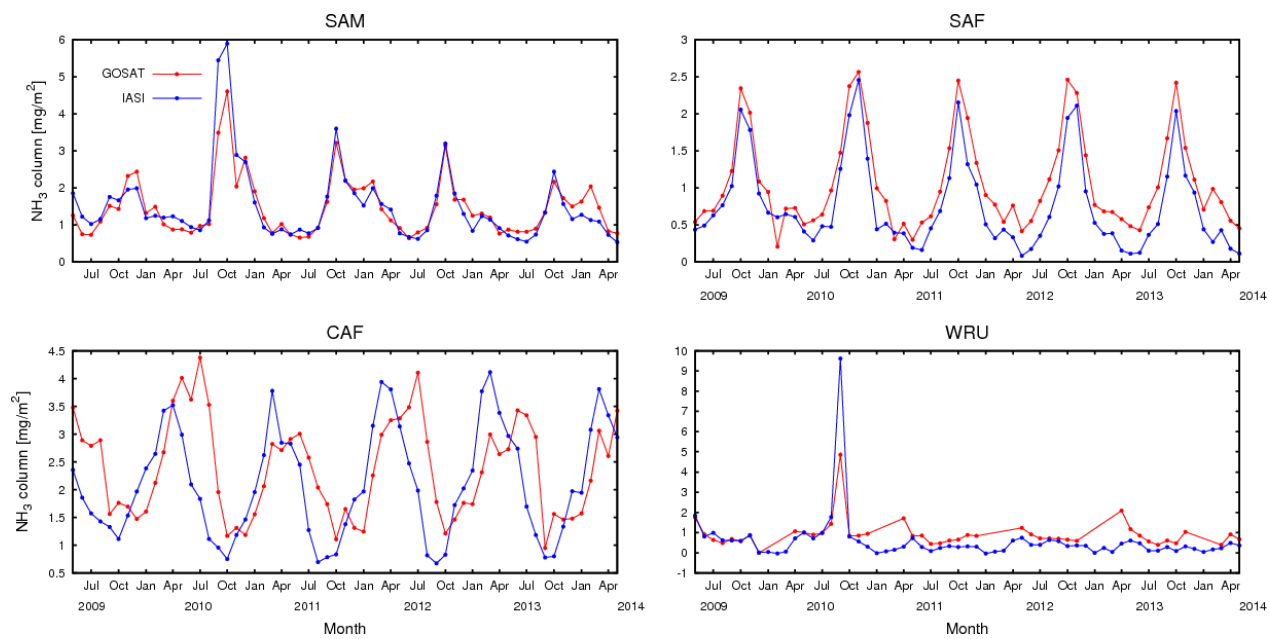


**Figure 10:** Same as Figure 9, but for the biomass burning areas.

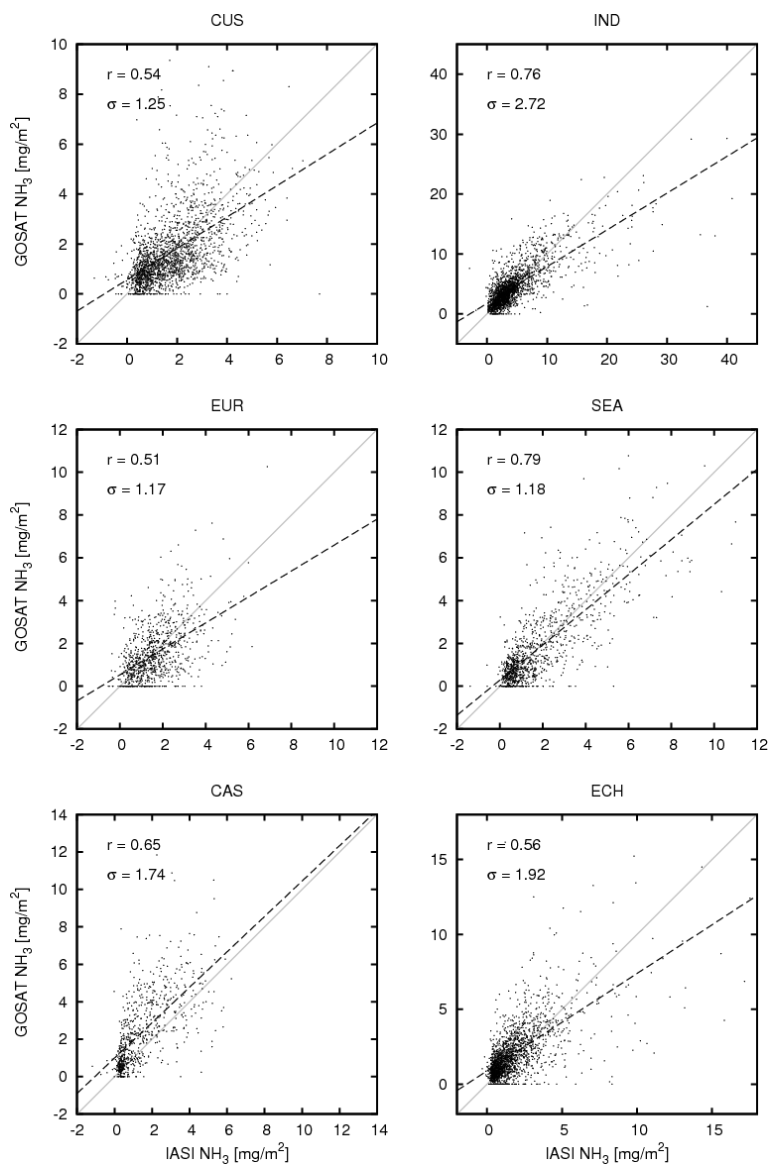


**Figure 11:** Scatter plots of the monthly averaged columnar ammonia concentrations within  $2.5^\circ \times 2.5^\circ$  grids obtained by the GOSAT and IASI over the agricultural source areas.

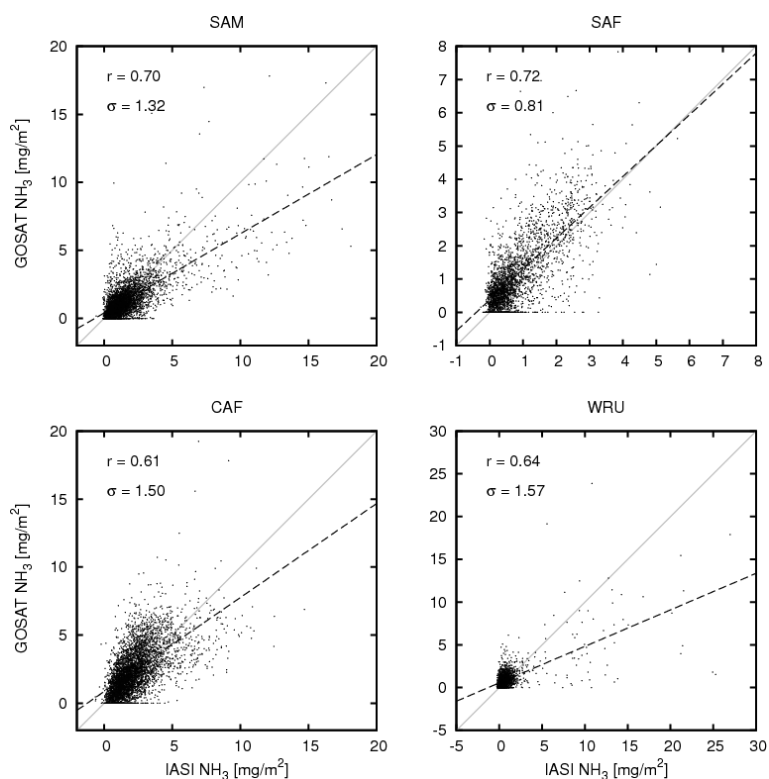
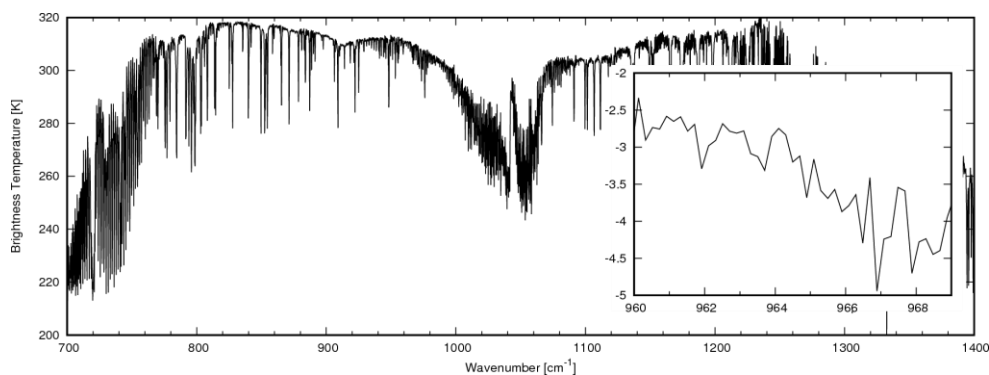
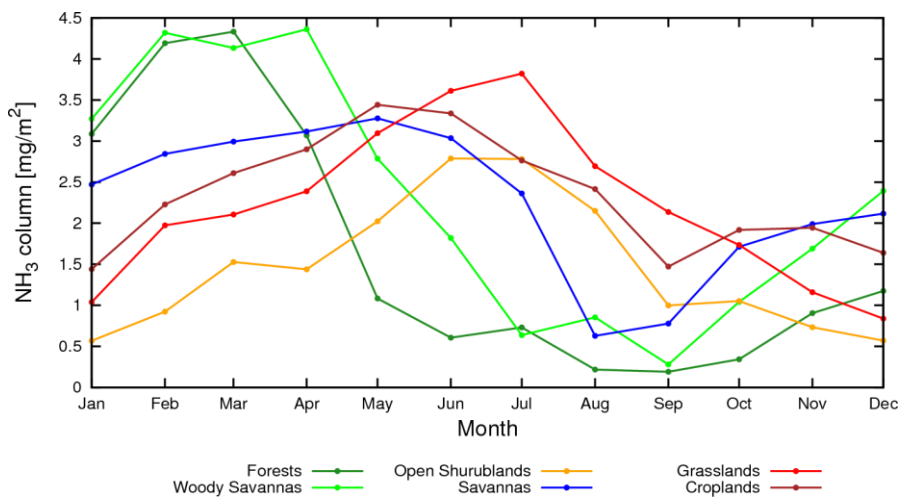


Figure 12: Same as Figure 11, but for the biomass burning source areas.



- 5 **Figure 13** An example of the observed spectra by the GOSAT affected by dust aerosols at (0.86°E, 29.17°N) on 22 July 2010, the residuals between the observed spectra and the one calculated without NH<sub>3</sub> (right inside).



**Figure 14:** Monthly variations of columnar ammonia concentrations from the GOSAT for the study period over forests, woody savannas, open shrublands, savannas, grasslands, and croplands classified by the MODIS product in CAF.